Irradiation-induced hardening in fusion relevant tungsten grades with different initial microstructures

ChihCheng Chang[a,b*], Dmitry Terentyev[a], Aleksandr Zinovev[a], Wouter Van Renterghem[a], Chao Yin[c], Patricia Verleysen[d], Thomas Pardoen[b], Monika Vilemova[e], Jiri Matějíček[e]

[a] Structural Materials Group, Institute of Nuclear Materials Science, SCK•CEN, 2400 Mol, Belgium
[b] Institute of Mechanics, Materials and Civil Engineering, UCLouvain, 1348 Louvain-la-Neuve, Belgium
[c] School of Nuclear Science and Technology, University of Science and Technology of China, Hefei, People's Republic of China
[d] Department of Department of Electromechanical, Systems & Metal Engineering, Ghent University, 9052 Ghent, Belgium
[e] Institute of Plasma Physics, Prague, Czech Republic

Keywords: Tungsten, Neutron irradiation, Irradiation hardening, microstructure

Abstract

The development of advanced tungsten grades able to tolerate irradiation damage combined with thermo-mechanical loads is important for design of plasma-facing components for DEMO. The material microstructure (i.e. grain size, dislocation density, sub grains, texture) is defined by manufacturing and post heat treatment processes. In turn, the initial microstructure might have an important influence on the accumulation of neutron damage because irradiation defects interact with microstructural defects evolving into a new microstructural state. In this work, the microstructure and hardness of four tungsten grades is assessed before and after neutron irradiation performed at 600, 1000 and 1200 °C, up to a dose of ~1.2 dpa. Experimental characterization involves hardness testing, energy dispersive spectroscopy, electron backscatter diffraction, and transmission electron microscopy. The investigated grades include Plansee and AT&M ITER specification tungsten, as well as fine grain tungsten produced by spark plasma sintering, and ultra-fine grain tungsten reinforced with 0.5 wt% ZrC particles.

1. Introduction

Tungsten is selected as armor and structural material for plasma facing components (PFCs) (i.e. divertors, first wall) in fusion devices due to its outstanding thermal properties, low erosion rate, and other attractive properties [1-3]. A relatively high ductile to brittle transition temperature (DBTT) is a concern. The DBTT of tungsten in non-irradiated state is 300-400°C depending on manufacturing route and loading condition (see e.g. [4-6]). Furthermore, exposure to 14 MeV neutron and high heat flux/thermal loads will degrade the bulk properties [7-9] and eventually cause cracking phenomena at PFC surface [10] which is the so-called irradiation embrittlement. To optimize the mechanical properties, many efforts are devoted in recent decades and several methods are implemented [11-17]. There are three mainstream ways to improve tungsten: (i) by cold rolling/thermal mechanical processing, (ii) by solid solution, for example by adding rhenium (Re), (iii) by grain size refinement and grain boundaries stabilization using strengthened particles (carbides, oxide dispersion strengthened.

The material microstructure is determined by the fabrication and optimization processes. For example, after rolling/double hammering tungsten will exhibit elongated grains and after sparking plasma sintering (SPS) it will have fine equiaxed grains. The different microstructure may have a different response to the neutron irradiation and different types of accumulated irradiation-induced defects. These defects include voids, dislocation loops, and precipitates of which the relative density and size distribution will vary with irradiation conditions. The presence of these defects will cause irradiation embrittlement which can be characterized by a decrease of elongation capacity, a reduction of fracture toughness, and/or an increase of the DBTT [18]. However, the tests required to assess these properties are material and space-consuming in irradiation campaigns. Hardness measurements are more efficient tests in terms of time and cost (i.e. material, space usage in an irradiation capsule), and, moreover, hardness can be correlated with the yield stress [19-21]. Hence, the mechanism and interaction between initial microstructure and irradiation-induced defects can be studied by micro-hardness tests and micrographic analysis.

In this work, we perform a parametric study on four tungsten grades to understand the link between the initial microstructure and the irradiation-induced hardness. The neutron irradiation was performed in Belgian Reactor 2 (BR2), Mol, Belgium, and the investigated samples were irradiated face-to-face to ensure an equivalent irradiation history. The irradiation temperatures were 600, 1000 and 1200 °C, and the irradiation dose ranged from 0.2 to 1.2 dpa. The reference and irradiated samples are characterized by Vickers hardness and microstructural measurements to establish the link between the hardness change and the initial microstructure.

2. Materials and methods

The studied grades represent two categories, pure tungsten and particle-reinforced tungsten. For pure tungsten, there are two ITER specification products supplied by Plansee (referred to as IGP) [22,23], AT&M (referred to as ATW) [22,24] and the fine grain tungsten (referred to as FG) supplied by IPP Prague [25,26]. The particle reinforced tungsten consists of ultra-fine grains and it is alloyed with 0.5 wt% of ZrC (referred to as W-05ZrC) [16]. The W-0.5ZrC material is produced by rolling and subsequent thermal heat treatment. Table 1 summarizes the composition and manufacturing process of the studied tungsten grades.

The disk specimens of 11 mm diameter and 0.5 mm thickness were prepared for neutron irradiation and equivalent samples were investigated in non-irradiated conditions. The details of the irradiation campaign and results obtained for the IGP material were already reported in [27,28]. The irradiation was performed in a helium environment (at 1 bar pressure) within the BR2 reactor. The position of the specimens inside the capsule is secured by centering ceramic guiding rods in order to maintain the dedicated gap between the stack of specimens and capsule wall to achieve the required irradiation temperature. The capsules are embedded inside the fuel element, where the fast neutron (E > 0.1 MeV) flux is (1-5) x 10^{14} n/cm^2/s at a reactor power of 60 MW. The transmutation rate of Re is about 2 at.% Re per dpa unit. It is important to note that we don't expect any pressure-driven helium permeation during the irradiation as the He pressure is way much lower than one required for any measurable helium penetration in tungsten. Secondly, all studied materials have been fabricated and/or stress-relived at the temperature of 1200°C or even higher (the case of the FG grade). Hence, the sole thermal annealing is not expected to impact the microstructure in terms of grain growth and recrystallization, whereas the synergy of irradiation and annealing might provoke the grain growth. However, due to the high residual activity on the samples, the EBSD measurements are currently prohibited on the as-irradiated materials.

The micro-hardness tests are performed by Vickers indentation under a force of 200 gf at room temperature. The time to reach the maximum force and the hold time is 10 seconds each. Such an indent leaves a trace on the tungsten surface of about 20-30 µm. Given that the investigated materials have sub-grains or grains with dimensions comparable or smaller than the indentation volume, each measured hardness point covers the response of several grains. Typically, ten points are sufficient to obtain a standard deviation within 5% of the average value of the hardness.

For the microstructural measurements, the samples are ground with P4000 SiC paper. Electrolytic polishing is applied to prepare the final surface just prior to taking the EBSD scan. The electrolyte for electropolishing is 1.5 wt% NaOH solution, and the parameters are 25 V with a flow rate of 18 L/min in the mask area of 2 cm^2 for 1 minute at room temperature. The grain size, grain boundary misorientation angles are established from EBSD data analysis by using EDAX-TSL OIM analysis software.

The density of microstructural sinks (grain boundaries, precipitates and pores) is determined by methodology proposed in [27]. The elongated grains are approximated as ellipsoids, see Fig. 1. A and B_1 are the major and minor medium length values (in area fraction) given the projection of a grain on a plane perpendicular to the normal direction (ND). While B_2 and C are the major and minor medium length values for the projection on a plane normal to the longitudinal direction (LD).

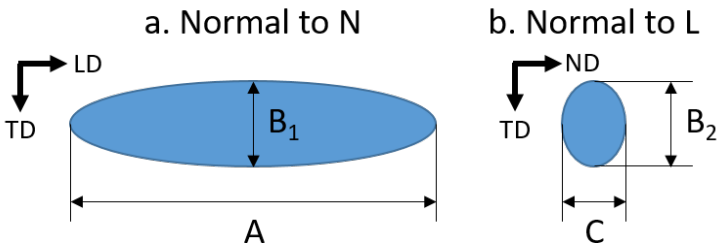

Fig. 1. The projected shape of an ellipsoidal grain on a plane (a) normal to ND and (b) normal to LD [27].

The volume (V_e), the approximated surface area (A_e), and the grain boundary surface area to volume ratio (S_v) of the elongated grain can be described as follows,

$$V_e = \frac{4}{3}\pi ABC, \tag{1}$$

$$A_e = 4\pi\left(\frac{A^pB^p + A^pC^p + B^pC^p}{3}\right)^{1/p}, \tag{2}$$

$$S_v = \frac{A_e}{2V_e}, \tag{3}$$

where p is a constant equal to 1.6075. From geometrical considerations, B should be equal to both B_1 and B_2. B is taken as the arithmetic mean value of B_1 and B_2.

The S_v of equiaxed grains can be described as,

$$S_v = \frac{3}{D50}, \tag{4}$$

where D50 is the equivalent medium diameter of grains.

$S_{v,tg}$ is the total surface-to-volume (S-V) ratio of grains surrounded by other grains with misorientaion angle (MA) larger than 2°.. $S_{v,g}$ is the S-V ratio of grains surrounded by high angle GBs (HAGBs) with MA > 15°. $S_{v,sg}$ is the S-V ratio of grains surrounded by low angle GBs (LAGBs) with MA between 2 to 15°, determined as:

$$S_{v,sg} = S_{v,tg} - S_{v,g}. \tag{5}$$

The ZrC particles and pores are identified by combining back-scattered electron (BSE) signal/EDS mapping [27] and SEM image of the polished FG sample [26], respectively. The corresponding values of $S_{v,particle}$ and $S_{v,pore}$ are calculated as:

$$S_{v,p} = \frac{6}{D50}. \tag{6}$$

3. Results and Discussion

The cube-projected EBSD maps and cumulative grain size distributions are shown in Fig. 2, and characteristic grain sizes together with particle/pore size are summarised in Table 2. As shown in Fig. 2a, 2b & 2c, the grains are elongated in the IGP, ATW and W-0.5ZrC products as expected due to the manufacturing process. The FG exhibits equiaxed grains, see Fig. 2d. IGP and ATW have, respectively, carrot- and pancake-like shape of grains with D50 being several tens of µm. D50 of W-0.5ZrC and FG is much smaller because of the specific production route [16,29].

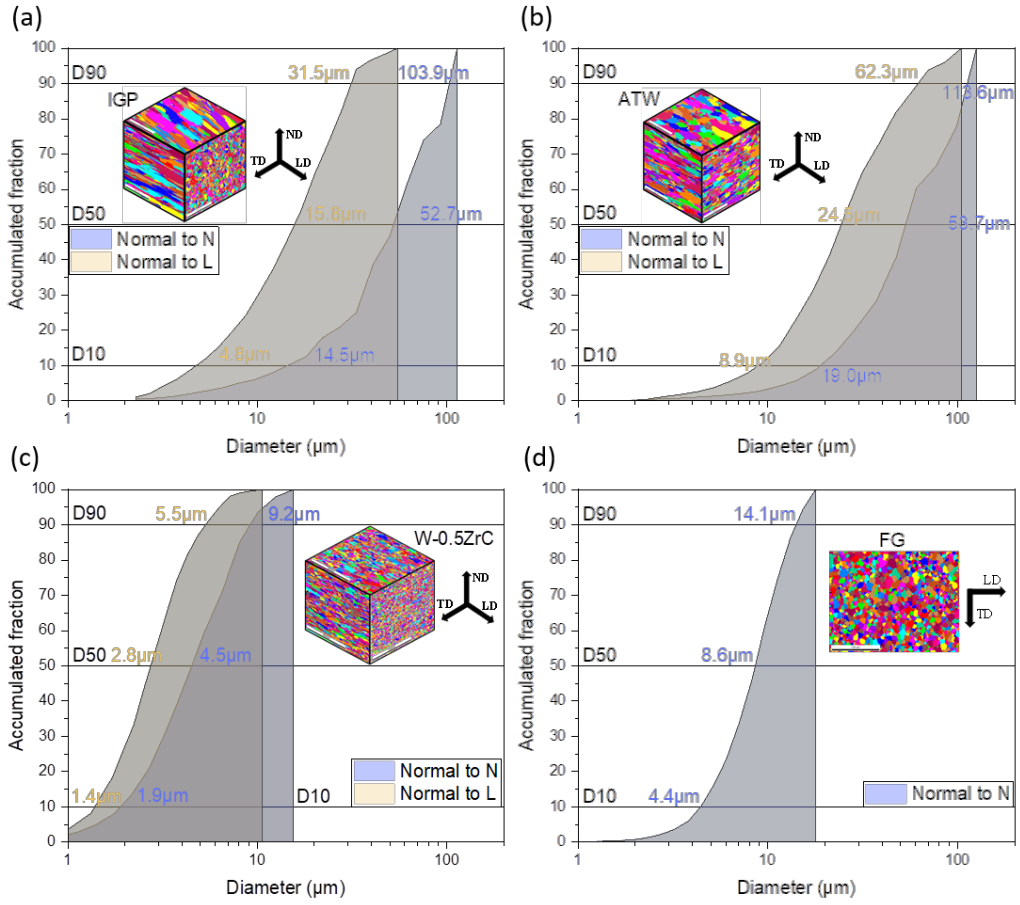

Fig. 2. Grain shape figure of tungsten grades and cumulative grain size distribution of planes normal to ND and LD (a) IGP; (b) ATW; (c) W-0.5ZrC; (d) FG.

Table 1. Dimensions of the grains and of the strengthening particles of different tungsten grades. D10 and D90 is equivalent 10% diameter and equivalent 90% diameter of grains respectively.

Materials	Composition	Manufacturing process	Equivalent diameter (µm)						
			Plane normal to	W grain			Particle (W-0.5ZrC) / Pore (FG)		
				D10	D50	D90	D10	D50	D90
IGP [27]	Pure W (>99.97 wt%)	Double hammering	ND	14.5	52.7	103.9	-	-	-
			LD	4.8	15.8	31.5	-	-	-
ATW	Pure W (>99.94 wt%)	Rolling	ND	19.0	53.7	113.6	-	-	-
			LD	8.9	24.5	62.3	-	-	-
W-0.5ZrC [27]	99.5 wt% W + 0.5 wt % ZrC	Rolling + TMT	ND	1.9	4.5	9.2	0.2	0.4	0.8
			LD	1.4	2.8	5.5	-	-	-
FG	Pure W (>99.97 wt%)	Spark Plasma Sintering (SPS), note that the material has 4% porosity	ND	4.4	8.6	14.1	0.7	1.0	1.6

The mean lengths of grain axes, as determined using EBSD measurements, are reported in Table 2. $S_{v,g}$, and $S_{v,sg}$ are then calculated using Eq. (3) and (5) for IGP, ATW and W-0.5ZrC products. $S_{v,g}$, and $S_{v,sg}$ for the FG are calculated with Eq. (4) and (5). Eq. (6) is applied to calculate the $S_{v,particle}$ for W-0.5ZrC and the $S_{v,pore}$ for FG. All the calculated values are reported in Fig. 3(a).

Table 2. The medium length of the major and minor axes of grains of IGP, ATW, W-0.5ZrC, and FG.

Materials	Medium length (µm)							
	Grains or sub-grains with misorientation > 2°				Grains with HAGBs			
	A	B_1	B_2	C	A	B_1	B_2	C
IGP [27]	3.9	1.6	2.0	1.2	77.1	10.0	12.5	4.8
ATW	4.4	1.9	2.4	1.3	41.9	16.7	22.2	6.6
W-0.5ZrC [27]	1.7	0.9	1.4	0.8	5.1	1.7	1.9	1.0

In Fig. 3(b) the reference hardness values are compared with the sink density and initial dislocation density taken from [30]. The IGP and ATW exhibit essentially similar $S_{v,g}$, $S_{v,sg}$ and dislocation density. It is thus not a surprise that IGP and ATW have a comparable hardness. W-0.5ZrC exhibits the highest sink density, dislocation density, and the highest hardness, which is expected. The FG has a rather high $S_{v,t}$ value due to the presence of pores. However, FG exhibits the lowest hardness due to the low dislocation density and absence of LAGBs [31].

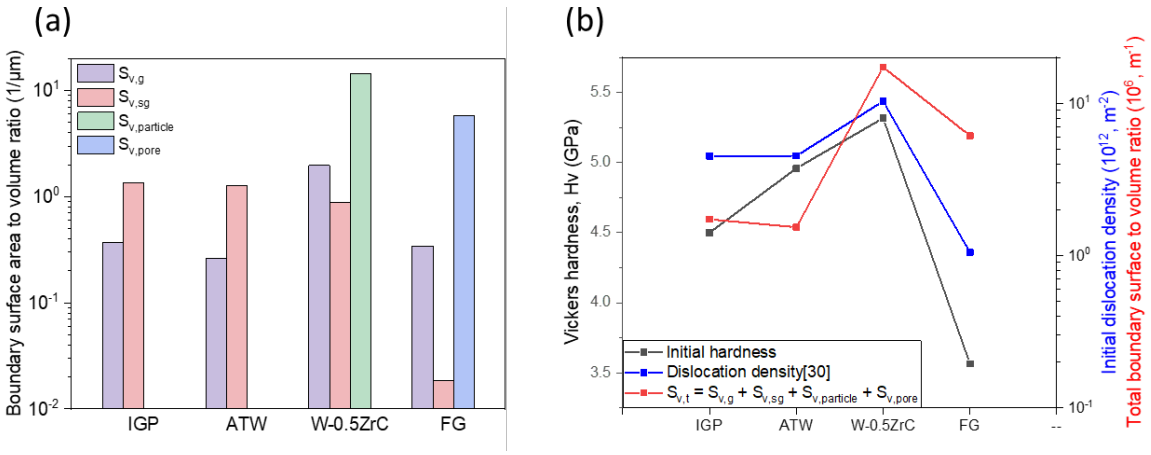

Fig. 3. The effect of microstructure on initial hardness of studied tungsten grades. (a) Surface area to volume ratio of grain/subgrain/particle/pore and (b) initial hardness compared with $S_{v,t}$ and initial dislocation density.

Fig. 4 presents the variation of the hardness as a function of the neutron irradiation (ΔH, henceforth called irradiation hardening) as a function of dpa. Fig. 4(a) summarizes the results obtained with all the irradiation conditions, while Fig. 4(b) focuses on the results obtained at 1-1.2 dpa.

It is convenient to discuss the results obtained for different grades using ΔH for the IGP product as a baseline trend which is already presented in our earlier studies [27,28]. ΔH at T_{irr}=600°C increases with increasing dose as the density of irradiation defects such like dislocation loops (DL) and voids steadily rises [32]. At around 0.9-1 dpa, the $\Delta H_{v,IGP,600}$, $\Delta H_{v,IGP,1000}$ and $\Delta H_{v,IGP,1200}$ are comparable. This concurrent evolution presumably results from the interplay of the irradiation temperature and accumulation of voids, DLs and precipitates. Lower irradiation temperature promotes the accumulation of dislocation loops, while high temperature enhanced the formation of voids and precipitates, with the peak swelling at 800°C [33]. Given the one-dimensional nature of the DL diffusion, the microstructural defects such as dislocations and grain boundaries should effectively absorb DLs, thereby promoting conditions for the nucleation and growth of voids. The density of voids reaches the maximum around 800°C and then decreases due to thermally-activated dissolution and subsequent coarsening of voids [34].

The link between irradiation induced defects and hardness change can be empirically expressed as:

$$\Delta H_v = 3.20 M \alpha \mu b (ND)^{0.5}, \quad (7)$$

where the M is the Taylor factor which is 3.06 here for non-textured BCC polycrystalline metals [35], μ is the shear modulus of the matrix which is 161 GPa here for tungsten, b is the Burgers vector. α is the dislocation-defect interaction strength, which is low for DLs (α_{DLs} is ~0.15) and high for voids (α_{voids} is 0.25 to 0.4) [34]. N and D are the density and size of the defects, respectively. ΔH is determined as the sum of the contributions coming from DLs, voids and precipitates, and at T_{irr}=600°C the high density of loops would provide a main contribution, while at T_{irr} > 1000°C, N_{DLs} will decrease by one to two orders (compared to 600°C) thus making less numerous but stronger voids to be the main contributor [28]. This mainly explains why at moderate irradiation dose (i.e. ~ 1 dpa) the ΔH is comparable at 600, 1000 and 1200°C.

Although ATW and IGP exhibit a very similar initial microstructure and chemical composition, ΔH in ATW at T_{irr}=600°C is considerably lower at 0.1-0.7 dpa. Unfortunately, no data is available for 1 dpa for this

material. The lower ΔH in the ATW is well outside the standard deviation measurements and cannot be explained by variation of the irradiation history as the samples were irradiated face-to-face. Hence, the reasons for the lower ΔH in ATW are not clear. One possible explanation is the spatial distribution of interstitial impurities such as oxygen, nitrogen, carbon [36], which are known to exhibit strong interaction with dislocation loops and vacancies [37,38].

ΔH measured for the FG at T_{irr}=600°C/0.2 dpa and T_{irr}=1000°C/0.7 dpa also reveals rather low values if compared with the trend curve drawn for the IGP. This result may be explained by high density of pores (i.e. high $S_{v,pore}$) which act as sinks for DLs as well as suppress nucleation of new voids by absorbing vacancies and their small 3D-migrating clusters [39,40].

Fig. 4(b) reveals the irradiation hardening at 1~1.2 dpa, the upper dose limit studied here. In particular, it is interesting to compare materials with relatively high and low sink density i.e. W-0.5ZrC and IGP/ATW. At T_{irr}=600°C, $\Delta H_{v,W0.5ZrC}$ is 20% lower than $\Delta H_{v,IGP}$, while the irradiation hardening of these two materials is almost identical at T_{irr}= 1200°C. This result demonstrates that the effect of the sinks is less important at high irradiation temperature. In turn, it is explained by the in-situ recovery of the damage that occurs thanks to thermally activated processes, i.e. void dissolution, detrapping of the loops from dislocation lines, etc. [41]. Even though Fig.4 reports a relative increase of the hardness, plotting the absolute values of the hardness after the irradiation yields to the same observations and outcomes as discussed above.

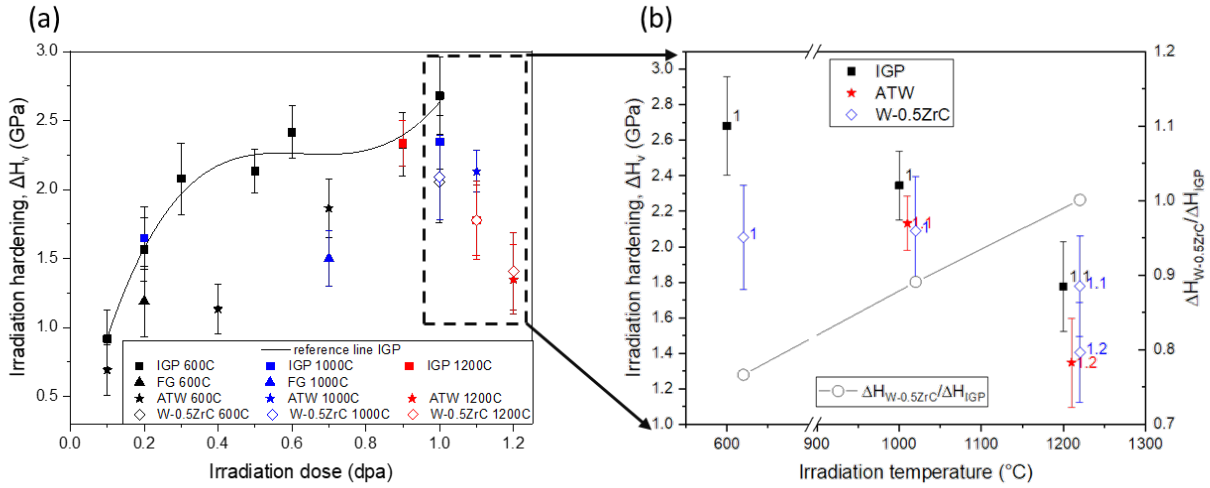

Fig. 4. (a) Variation of irradiation hardening as a function of irradiation does in dpa. (b) Left axis displays the irradiation hardening vs. irradiation temperature, right axis shows the ratio $\Delta H_{v,W-0.5ZrC} / \Delta H_{v,IGP}$.

4. Conclusions

Based on the presented results and discussed correlation between microstructural sink density and irradiation-induced hardness, the following conclusions can be made:

1) Although ATW and IGP products exhibit essentially similar microstructures and chemical purities, the irradiation hardening registered in the ATW at T_{irr} =600°C at 0.4 dpa and 0.7 dpa is considerably lower. The reasons for this difference are not clear at the moment. Spatial location of the main interstitial impurities (carbon, nitrogen, oxygen) and their absolute concentration might help to reconcile the difference. Comparative TEM studies of the irradiation microstructures are also required to deduce the reasons for the observed deviation.
2) The ratio of the irradiation hardening in W-0.5ZrC and IGP grades (i.e. high and low sink density materials) approaches unity with increasing the irradiation temperature. This shows that the effect of microstructural sinks does not dominate at high irradiation temperature (~T_m/3), while a high sink density evidently helps the suppression of the irradiation hardening at T_{irr}=600°C (~T_m/6).
3) FG tungsten exhibits rather low irradiation hardening compared to other studied materials. We suspect that high density of pores acted as additional sinks for the irradiation defects.

Acknowledgments

This work has been carried out within the framework of the EUROfusion Consortium and has received funding from the Euratom research and training programme 2014-2018 and 2019-2020 under grant agreement No 633053. The views and opinions expressed herein do not necessarily reflect those of the ITER Organization or of the European Commission. The work was partially supported by FOD fusion grant.

Reference

1. Barrett TR, Ellwood G, Pérez G, Kovari M, Fursdon M, Domptail F, et al. Fusion Engineering and Design. 2016;109-111:917-24.
2. You JH, Visca E, Barrett T, Böswirth B, Crescenzi F, Domptail F, et al. Nuclear Materials and Energy. 2018;16:1-11.
3. Pitts RA, Bonnin X, Escourbiac F, Frerichs H, Gunn JP, Hirai T, et al. Nuclear Materials and Energy. 2019;20:100696.
4. Giannattasio A, Yao Z, Tarleton E, Roberts SG. Philosophical Magazine. 2010;90(30):3947-59.
5. Gludovatz B, Wurster S, Hoffmann A, Pippan R. International Journal of Refractory Metals and Hard Materials. 2010;28(6):674-8.
6. Rupp D, Weygand SM. Philosophical Magazine. 2010;90(30):4055-69.
7. Steichen JM. Journal of Nuclear Materials. 1976;60(1):13-9.
8. Gorynin IV, Ignatov VA, Rybin VV, Fabritsiev SA, Kazakov VA, Chakin VP, et al. Journal of Nuclear Materials. 1992;191-194:421-5.
9. Yin C, Terentyev D, Zhang T, Petrov RH, Pardoen T. Journal of Nuclear Materials. 2020;537:152226.
10. Li M, You J-H. Fusion Engineering and Design. 2015;101:1-8.

11. Kurishita H, Arakawa H, Matsuo S, Sakamoto T, Kobayashi S, Nakai K, et al. MATERIALS TRANSACTIONS. 2013;54(4):456-65.
12. Mutoh Y, Ichikawa K, Nagata K, Takeuchi M. Journal of Materials Science. 1995;30(3):770-5.
13. Rieth M, Dudarev SL, Gonzalez De Vicente SM, Aktaa J, Ahlgren T, Antusch S, et al. Journal of Nuclear Materials. 2013;432(1-3):482-500.
14. Lied P, Bonnekoh C, Pantleon W, Stricker M, Hoffmann A, Reiser J. International Journal of Refractory Metals and Hard Materials. 2019;85:105047.
15. Nogami S, Hasegawa A, Fukuda M, Watanabe S, Reiser J, Rieth M. Fusion Engineering and Design. 2020;152:111445.
16. Xie ZM, Liu R, Miao S, Yang XD, Zhang T, Wang XP, et al. Scientific Reports. 2015;5(1):16014.
17. Fukuda M, Nogami S, Yabuuchi K, Hasegawa A, Muroga T. Fusion Science and Technology. 2015;68(3):690-3.
18. Xiao X. Fundamental Mechanisms for Irradiation-Hardening and Embrittlement: A Review. Metals. 2019;9(10):1132.
19. Yao WZ, Wang P, Manhard A, Krill CE, You JH. Materials Science and Engineering: A. 2013;559:467-73.
20. Yao WZ, Krill CE, Albinski B, Schneider HC, You JH. Journal of Materials Science. 2014;49(10):3705-15.
21. Miyazawa T, Garrison LM, Geringer JW, Fukuda M, Katoh Y, Hinoki T, et al. Journal of Nuclear Materials. 2020;529:151910.
22. Hirai T, Panayotis S, Barabash V, Amzallag C, Escourbiac F, Durocher A, et al. Nuclear Materials and Energy. 2016;9:616-22.
23. Wirtz M, Linke J, Loewenhoff T, Pintsuk G, Uytdenhouwen I. Physica Scripta. 2016;T167:014015.
24. Yin C, Terentyev D, Pardoen T, Petrov R, Tong Z. Materials Science and Engineering: A. 2019;750:20-30.
25. Terentyev D, Vilémová M, Yin C, Veverka J, Dubinko A, Matějíček J. International Journal of Refractory Metals and Hard Materials. 2020;89.
26. Matějíček J, Veverka J, Yin C, Vilémová M, Terentyev D, Wirtz M, et al. Journal of Nuclear Materials. 2020;542:152518.
27. Yin C, Terentyev D, Dubinko A, Zhang T, Wirtz M, Antusch S, et al. Nuclear Fusion. 2021;61:6.
28. Terentyev D, Yin C, Dubinko A, Chang CC, You JH. International Journal of Refractory Metals and Hard Materials. 2021;95:105437.
29. Matějíček J, Vilémová M, Veverka J, Kubásek J, Lukáč F, Novák P, et al. Metals. 2019;9(8):879.
30. Dubinko A, Yin C, Terentyev D, Zinovev A, Rieth M, Antusch S, et al. International Journal of Refractory Metals and Hard Materials. 2021;95.
31. Graça S, Colaço R, Carvalho PA, Vilar R. Materials Letters. 2008;62(23):3812-4.
32. Castin N, Bakaev A, Bonny G, Sand AE, Malerba L, Terentyev D. Journal of Nuclear Materials. 2017;493:280-93.
33. Matolich J, Nahm H, Moteff J. Scripta Metallurgica. 1974;8(7):837-41.
34. Hu X, Koyanagi T, Fukuda M, Kumar NAPK, Snead LL, Wirth BD, et al. Journal of Nuclear Materials. 2016;480:235-43.
35. Stoller RE, Zinkle SJ. Journal of Nuclear Materials. 2000;283-287:349-52.
36. Castin N, Bonny G, Bakaev A, Ortiz CJ, Sand AE, Terentyev D. Journal of Nuclear Materials. 2018;500:15-25.
37. Kong X-S, You Y-W, Song C, Fang QF, Chen J-L, Luo GN, et al. Journal of Nuclear Materials. 2012;430(1-3):270-8.
38. Kong X-S, You Y-W, Fang QF, Liu CS, Chen J-L, Luo GN, et al. Journal of Nuclear Materials. 2013;433(1-3):357-63.

39. Bringa EM, Monk JD, Caro A, Misra A, Zepeda-Ruiz L, Duchaineau M, et al. Nano Letters. 2012;12(7):3351-5.
40. Fu EG, Caro M, Zepeda-Ruiz LA, Wang YQ, Baldwin K, Bringa E, et al. Applied Physics Letters. 2012;101(19):191607.
41. Was GS. Fundamentals of radiation materials science. Springer. 2016.